QUARTERLY JOURNAL OF THE ROYAL METEOROLOGICAL SOCIETY
Q. J. R. Meteorol. Soc. **133**: 83–99 (2007)
Published online in Wiley InterScience
(www.interscience.wiley.com) DOI: 10.1002/qj.20

RMetS
ROYAL METEOROLOGICAL SOCIETY

Impacts of initial condition errors on mesoscale predictability of heavy precipitation along the Mei-Yu front of China

Naifang Bei[a,b] and Fuqing Zhang[a]*
[a] *Department of Atmospheric Sciences, Texas A&M University, College Station, Texas, USA*
[b] *Institute of Atmospheric Physics, Chinese Academy of Sciences, Beijing, China*

ABSTRACT: Summertime heavy precipitation associated with the quasi-stationary Mei-Yu front often causes severe flooding along the Yangtze river basin in China. This study explores the mesoscale predictability of one such event near Wuhan, the capital city of Hubei Province. The 20–21 July rainfall event contributed to making the 1998 flood season the worst in this region since 1954. Various sensitivity experiments were performed to examine the impact of both realistic and idealized initial condition uncertainties of different scales and amplitudes on the prediction of the mesoscale precipitation systems along the Mei-Yu front. While it is found that mesoscale model simulations initialized with global analyses at a 36-h lead time can depict the evolution of the synoptic environment reasonably well, there are large variations between different experiments in the prediction of the mesoscale details and heavy precipitation of this event. It was also found that larger-scale, larger-amplitude initial uncertainties generally led to larger forecast divergence than did uncertainties of smaller scales and small amplitudes. However, the forecast errors induced by perturbations of the same amplitude but at different scales are very similar if the initial error is sufficiently small. Error growth is strongly nonlinear and small-amplitude initial errors, which are far smaller than those of current observational networks, may grow rapidly and quickly saturate at smaller scales. They subsequently grow upscale, leading to significant forecast uncertainties at increasingly larger scales. In agreement with previous studies, moist convection is found to be the key to the rapid error growth leading to limited mesoscale predictability. These findings further suggest that, while there is significant scope for improving forecast skill by improving forecast models and initial conditions, mesoscale predictability of such a heavy precipitation event is inherently limited. Copyright © 2007 Royal Meteorological Society

KEY WORDS atmospheric predictability; qualitative precipitation forecast; initial condition uncertainties; error growth

Received 30 January 2006; Revised 25 August 2006; Accepted 12 September 2006

1. Introduction

The concept of limited predictability due to instability in dynamic systems was first introduced by Maxwell (1876). Thompson (1957) described atmospheric predictability as the sensitivity to initial condition and model errors in numerical weather prediction models. Lorenz (1963) showed the apparent loss of predictability in a low-order model of atmospheric flow, and Lorenz (1969) used a two-dimensional (2D) closure model to quantify multi-scale predictability and show the slow inverse cascade of errors from small to large scales. The loss of predictability due to upscale error transfer was further verified by Leith and Kraichnan (1972), using an improved closure model.

Research on mesoscale predictability began with Anthes *et al*. (1985), which found little forecast divergence from simulations using different initial conditions in a limited area mesoscale model. The slow growth of forecast differences in their simulations was later attributed to the combined effects of using fixed lateral boundary conditions, relatively strong numerical dissipation, and unbalanced initial perturbations (Errico and Baumhefner, 1987; Vukicevic and Errico, 1990). Recently, Zhang *et al*. (2002, 2003) demonstrated the possible influence of initial errors of small amplitude and scale on the numerical prediction of the 'surprise' snowstorm of 24–25 January 2000. They found that initial errors grew rapidly at scales below 200 km in the presence of moist processes and were characterized by upscale growth. The above results from real case studies were subsequently generalized in Tan *et al*. (2004) by their examination of error growth in idealized baroclinic waves amplifying in a conditionally unstable atmosphere.

Compared with cool-season weather systems with strong baroclinicity, the current skill of operational quantitative precipitation forecasts (QPF) during the warm season is low, especially for heavy precipitation events (Olson *et al*., 1995; Fritsch *et al*., 1998). Zhang *et al*. (2006) examined the mesoscale predictability of a warm-season extreme precipitation event over south-central Texas that began on 29 June 2002 and lasted until 7 July 2002. It was found that the high-resolution, convective-resolving simulation did not produce the best simulation or forecast, and both the realistic initial

* Correspondence to: Fuqing Zhang, Department of Atmospheric Sciences, Texas A&M University, College Station, TX 77845-3150, USA.
E-mail: fzhang@tamu.edu

condition uncertainty and model errors resulted in large forecast errors for this warm-season flooding event. In addition, the authors further demonstrated that small-scale, small-amplitude initial errors, such as those in the form of undetectable random noise, can grow rapidly and subsequently contaminate the short-term deterministic mesoscale forecast within 36 h. Faster error growth, especially at smaller scales in the presence of parameterized moist convection, was also found by Ehrendorfer *et al.* (1999). The impacts of moist convection on the limit of mesoscale predictability demonstrated in these recent studies are consistent with what was foreseen by Lorenz (1969) and with recent findings of faster error growth from smaller scales in Buizza *et al.* (2003) and Simmons and Hollingsworth (2002). The limited deterministic predictability of such events thus illustrates the need for mesoscale probabilistic forecasts (Zhang *et al.*, 2006).

For synoptic-scale predictability, scale-dependent error growth processes were recently investigated by Tribbia and Baumhefner (2004) in a coarse-resolution global model using truncated perturbations at different scales. They found that errors limited to synoptic and larger scales grew at a nearly identical rate to errors that were not band-limited. Errors limited to smaller scales required additional time for the inertial cascade processes to seed the baroclinically active regions of the spectrum before growth could proceed. They argued that synoptic-scale errors organize within synoptic structures and amplify, extracting energy only from the larger-scale background flow. The inverse cascade in the traditional view (Lorenz, 1984) thus becomes of lesser importance.

This study explores the mesoscale predictability of a warm-season heavy rainfall event associated with the quasi-stationary Mei-Yu front along the Yangtze river basin of east-central China with a high-resolution, limited area model. This is a typical heavy precipitation event occurring in a typical Mei-Yu synoptic environment. Complementary to the aforementioned studies, we are particularly interested in examining the impact of both realistic and idealized initial condition uncertainties at different scales and amplitudes on the mesoscale prediction of this event and its attendant heavy precipitation. An overview of this flooding event is provided in the next section. Section 3 describes the model and experimental design. Section 4 presents the results of the unperturbed simulations with a focus on the 10-km control run. Sensitivity to realistic initial uncertainties is presented in Section 5. The results with idealized perturbations are given in Section 6. A discussion and conclusions are presented in Section 7. Since this is a typical warm-season rainfall event and the idealized initial perturbations and area-integrated diagnostics are used, the results derived from this single study may be common to many other similar types of weather systems.

2. Synoptic overview of the flooding event

The rainy period of mid-to-late spring through to early-to-mid-summer in East Asia is typically caused by a quasi-stationary, east–west orientated frontal zone often referred to as the Mei-Yu front, which often causes severe flooding along the Yangtze river basin in China and is one of the most significant weather systems for the hydrological cycle in the East Asia monsoon region. The Mei-Yu front is characterized by weak temperature gradients and strong moisture gradients in the lower troposphere (Ding, 1992), which, is different from that of typical mid-latitude fronts. The front is usually shallow and slopes rapidly with height, which is typically accompanied by a low-level cyclonic wind shear line to the north and a well-defined, synoptic-scale, low-level jet (LLJ) to the south of the shear line (Chen *et al.*, 1998). The LLJ may destabilize the environment through transporting warm moist air northwards in the lower levels (Chen, 1983), and may trigger convective development through inducing upward motion (as part of the secondary circulation) at its left exit region (Chen, 1982). Similar weak quasi-stationary fronts are also present over central USA (and possibly other areas), although these are much more transient and much less pronounced (Carbone *et al.*, 2002).

This study explores the mesoscale predictability of one such Mei-Yu front heavy precipitation event on 20–21 July 1998 near Wuhan, the capital city of Hubei Province. This rainfall event contributed to making the 1998 flood season the worst in this region since 1954 (Zhao *et al.*, 1998). For example, an observational analysis of the 24-h accumulated precipitation from 12 : 00 UTC 20 July to 12 : 00 UTC 21 July 1998 is shown in Figure 1(a) (the simulated results in Figure 1(b)–(d) will be discussed later), and the time evolution of the observed hourly accumulated precipitation averaged over 35 stations around the extreme local rainfall maximum near Wuhan in the east of Hubei Province is shown in Figure 2 (all geographical locations referred hereafter are shown in Figure 1(a)). The maximum hourly rainfall near Wuhan reached 88.4 mm at 00 : 00 UTC 21 July, and the 24-h accumulated precipitation maxima near Wuhan and also in northeastern Guizhou Province were larger than 200 mm (Figure 1(a)).

The large-scale environment over the Yangtze river basin was generally favourable for the development of mesoscale weather systems on 20–21 July 1998 due to the presence of several upper level features. At 700 hPa, from 00 : 00 UTC 20 to 00 : 00 UTC 21 July, an east–west orientated quasi-stationary shear line existed along the basin at 700 hPa, along which a subsynoptic-scale, low-pressure centre was initially located at (29 °N, 107 °E) in the east of Sichuan Province gradually moved eastward (Figure 3(a)). A corresponding 500-hPa shortwave quasi-stationary trough was located at (25–35 °N, 105 °E) near the north of Sichuan Province and the south of Shanxi Province (Figure 3(b)). A series of mesoscale convective systems developed along the mid-to-low-level convergence boundary and progressed from west to east. Among these systems, a mesoscale convective vortex developed near Wuhan and led to heavy precipitation. The setting described above, along with the mostly

DOI: 10.1002/qj

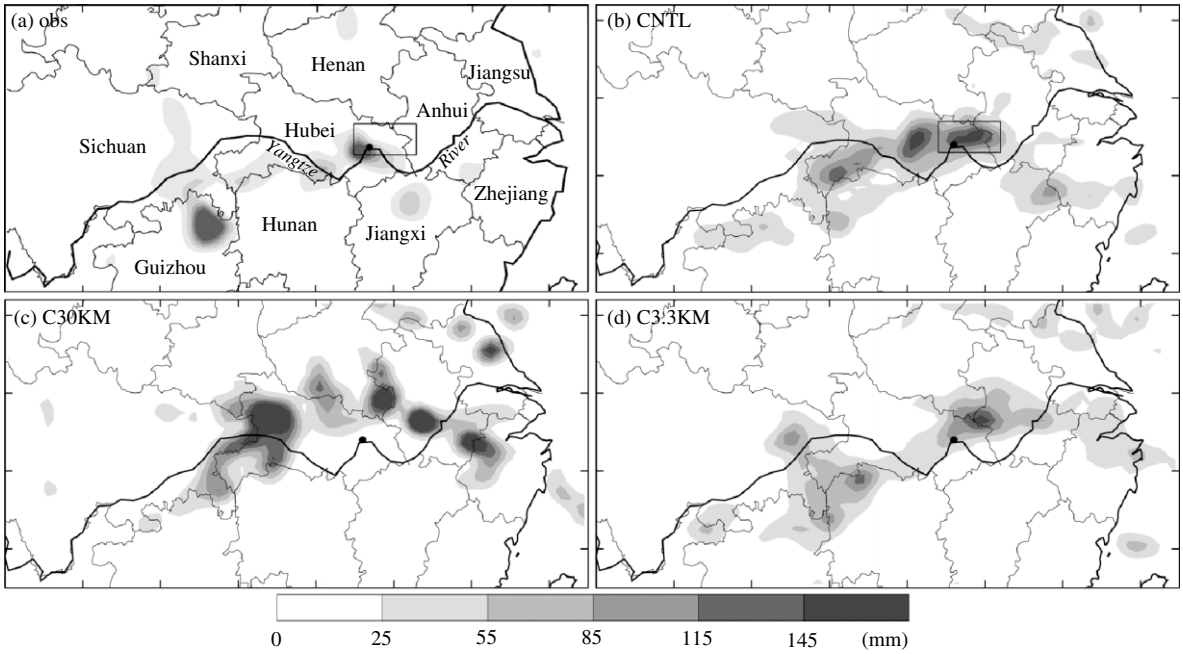

Figure 1. The 24-h accumulated precipitation (mm) from 12 : 00 UTC 20 to 12 : 00 UTC 21 July 1998 for (a) observational analysis and simulations by (b) CNTL, (c) C30KM and (d) C3.3KM with a 36-h lead time plotted on the 30-km domain (D1). The Chinese provinces along the Yangtze River are labelled in (a). The black dot denotes the location of the Wuhan station and the distance between tick marks is 300 km in this and subsequent figures.

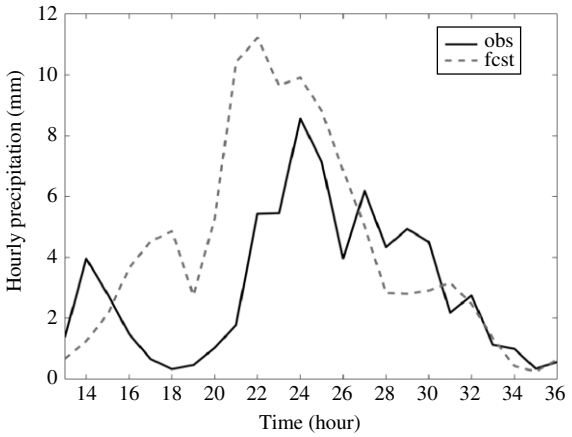

Figure 2. Time evolution of hourly-accumulated precipitation (mm) from observations (solid line, averaged over 35 stations near Wuhan) and CNTL simulation (dashed line, averaged over the small rectangular box denoted in Figure 1(a)) from 13 : 00 UTC 20 to 12 : 00 UTC 21 July 1998.

diffluent 200 hPa flow over the Yangtze river basin and a strong LLJ providing an abundant supply of water vapour (not shown), is a typical synoptic environment for heavy precipitation during the Mei-Yu season in central-eastern China (Ding, 1992; Chen *et al*., 1998; Bei and Zhao, 2002a).

Even after using numerical weather prediction models in hindsight, it is difficult to identify reliable predictors to forecast the heavy rainfall event (Bei and Zhao, 2002b, Bei *et al*., 2002). The purpose of this paper is to explore the impacts of initial condition uncertainties at different scales and different amplitudes on the prediction of this event and its attendant heavy precipitation.

3. Model description and experimental design

The NCAR/PSU non-hydrostatic mesoscale model MM5 version 3 (Dudhia, 1993) was used for this study. The unperturbed control simulation (hereafter referred to as 'CNTL') employs two horizontal domains (D1 and D2) with two-way nesting initialized at 00 : 00 UTC 20 July 1998 and with initial and boundary conditions derived from the $2.5^\circ \times 2.5^\circ$ global analyses of the European Centre for Medium-Range Weather Forecasts (ECMWF) which have been reanalysed with standard surface and sounding observations using the standard objective analysis tools available in MM5. The 30-km coarse domain employs the 190×120 horizontal grid points that cover most of China and the 10-km nested domain has 271×181 horizontal grid points (Figure 4). Both domains have 27 layers, half of which are below 700 hPa, in a stretched vertical coordinate. The Mellor–Yamada PBL scheme (Mellor and Yamada, 1982), Reisner microphysics scheme with graupel (Reisner *et al*., 1998) and Grell (1993) cumulus parameterization scheme were used in all experiments.

Experiments 'C30KM' and 'C3.3KM' were performed to examine the sensitivity of this extreme rainfall prediction to model resolution. C30KM is the same as CNTL except that it uses only the 30-km domain (D1, Figure 4). C3.3KM is the same as CNTL but with the addition of a two-way-nested 3.3-km domain with 271×271 grid points (D3, Figure 4). No cumulus parameterization was used for D3 in C3.3KM (Figure 4).

A series of experiments were subsequently designed to examine the impacts of realistic and idealized initial perturbations with different amplitudes and scales on the mesoscale predictability of this event. A list of these

DOI: 10.1002/qj

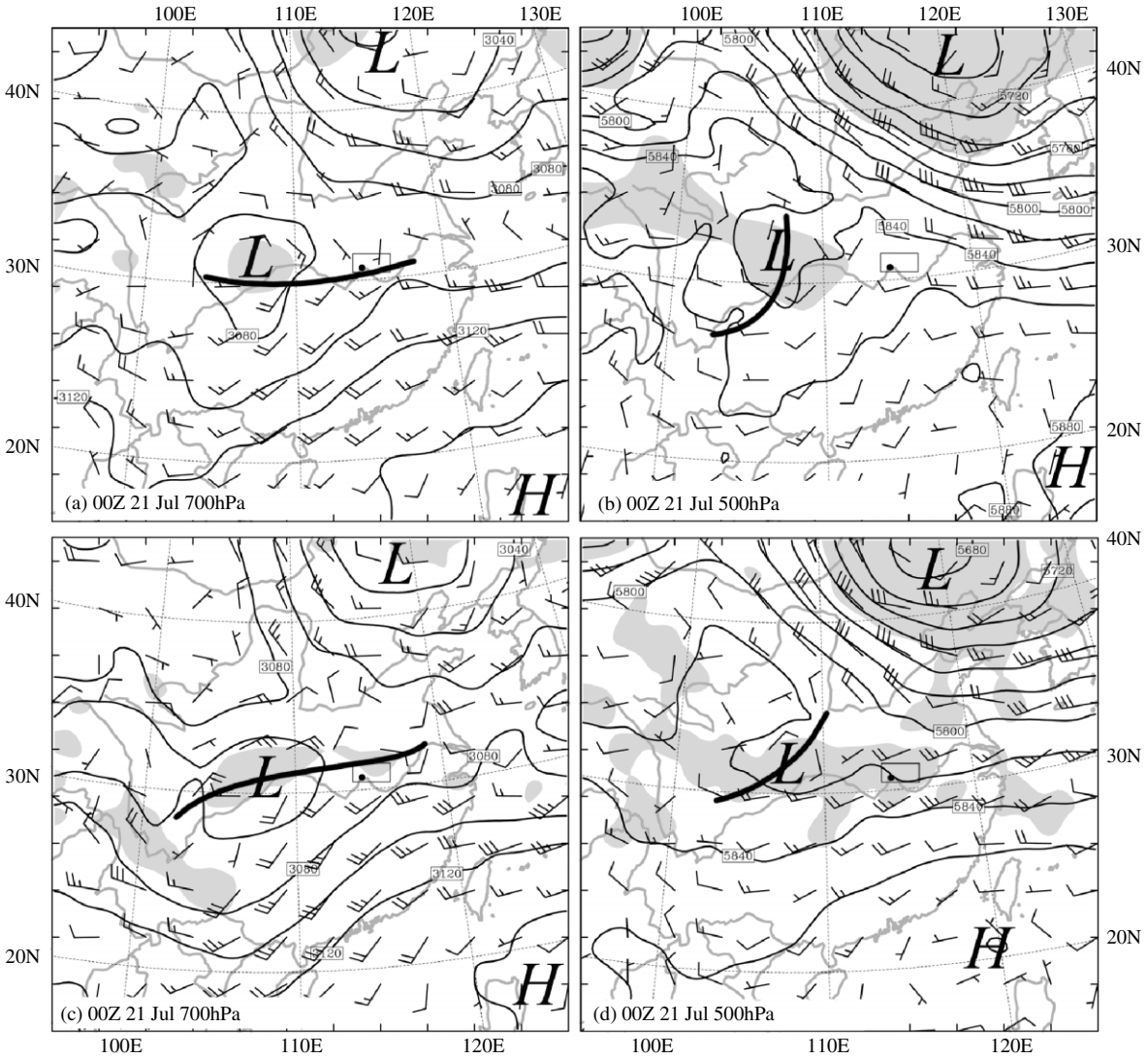

Figure 3. Horizontal winds (full barb, 5 m s^{-1}), geopotential heights (every 20 dam) and potential vorticity (>0.75 PVU shaded, PVU = 10^{-6} K m^2 kg^{-1} s^{-1}) valid at 00 : 00 UTC 21 July for observational analyses at (a) 700 hPa and (b) 500 hPa and the corresponding simulation by CNTL at (c) 700 hPa and (d) 500 hPa. The bold curves denote the locations of the mid-level trough and the low-level shear line.

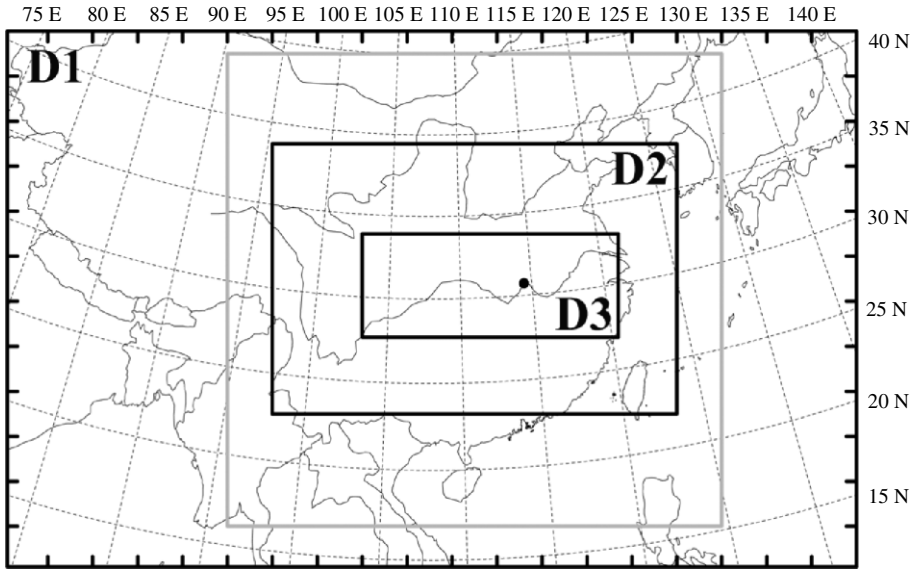

Figure 4. Configurations of the MM5 model domains. The horizontal grid spacing of domain 1 (D1), domain 2 (D2) and domain 3 (D3) is 30, 10 and 3.3 km, respectively. The grey box denotes the domain used in Figure 6.

DOI: 10.1002/qj

Table I. A list of sensitivity experiments with different initial perturbations.

Objectives	Experiments	Brief description
Sensitivity to initial data source	CNTL	Initial condition derived from ECMWF global analysis
	T106ic	Initial condition derived from NMC global analysis
Sensitivity to horizontal resolution	C30KM	As in CNTL, but use only D1 with 30-km grid spacing
	C3.3KM	As in CNTL, but use triply nested domains down to 3.3-km grid spacing
Sensitivity to lateral boundary condition	T106bc	As in CNTL, but lateral boundary conditions derived from NMC global analysis
Sensitivity to initial perturbations at different scales decomposed from difference between CNTL and T106ic	T106L	Perturbation only at scales greater than 1200 km
	T106M	Perturbation only at scales from 300 to 1200 km
	T106S	Perturbation only at scales smaller than 300 km
Sensitivity to the above decomposed initial perturbations but rescaled to the same amplitude (in terms of DTE) as difference between CNTL and T106ic	T106Ls	Rescaled perturbation at scales greater than 1200 km
	T106Ms	Rescaled perturbation at scales from 300 to 1200 km
	T106Ss	Rescaled perturbation at scales smaller than 300 km
Sensitivity to idealized perturbations with realistic initial amplitude	BAL	Large-scale balanced with the same amplitude as T106Ls
	UNB	Small-scale unbalance with the same amplitude as T106Ls
Sensitivity to smaller-amplitude idealized initial perturbations	BAL27%, BAL9%, BAL3%	As in BAL but with amplitude reduced to 27%, 9% or 3% of BAL
	UNB27%, UNB9%, UNB3%	As in UNB but with amplitude reduced to 27%, 9% or 3% of UNB
Sensitivity to effect of moisture in terms of latent heating/cooling (i.e. the 'fake-dry' experiments)	dryCNTL	As in CNTL but no latent heating/cooling allowed
	dryBAL(##%)	As in BAL(##%) but no latent heating/cooling allowed
	dryUNB(##%)	As in UNB(##%) but no latent heating/cooling allowed

experiments and a brief description are summarized in Table I. The details of each experiment are presented in the following sections, where their results are discussed.

4. Control simulations

Figure 1(b)–(d) shows the 24-h accumulated precipitation valid at 12 : 00 UTC 21 July 1998 (with a 36-h lead time) from the three control experiments (CNTL, C30KM and C3.3KM with effective grid spacing of 30, 10 and 3.3 km, respectively). All three simulations produced the observed east–west precipitation belt (Figure 1(a)) along the quasi-stationary Mei-Yu front, but significant differences existed (in terms of both precipitation amount and position) among simulations with different horizontal grid spacings.

The 10-km control experiment (CNTL), with a 36-h lead time, reasonably simulated the intensity and location of the heavy precipitation along the Yangtze river basin, but its precipitation was slightly to the north and east of the observed precipitation (Figure 1(b) *vs* Figure 1(a)). Moreover, the time evolution of hourly rainfall near Wuhan (averaged in the small box denoted in Figure 1(a)) simulated by CNTL compared favourably to the relevant observational average during the simulation period (Figure (2)). In addition, CNTL also reasonably well simulated the important synoptic features such as the east–west shear line at 700 hPa, the shortwave trough at 500 hPa and an attendant area of high potential vorticity over the Yangtze river basin (Figure 3(a)–(b) *vs* Figure 3(c)–(d)).

The highest resolution 3.3-km experiment (C3.3KM) did not produce the best results (Figure 1(d)). Degradations of higher-resolution forecasts similar to C3.3KM were also found by Gallus (2002) and Zhang *et al.* (2006). It is possible that, in cases such as this event, some subgrid-scale physical parameterizations are more suitable for use with coarser resolutions. Convective initiation in C3.3KM, which relies on grid-scale processes, may not be sufficient, since convection only becomes marginally resolvable with 3.3-km grid spacing (e.g. Done *et al.*, 2004).

DOI: 10.1002/qj

Since the 10-km CNTL experiment performed better than C30KM and C3.3KM (especially for the heavy precipitation), the following sensitivity experiments will be based on and compared with CNTL (and the perturbation or error referred to hereafter is thus defined as the difference from CNTL) unless otherwise specified.

5. Sensitivity to realistic initial condition uncertainties

It is very common for mesoscale models to derive their initial and boundary conditions from larger-scale or global models. The difference in the initial conditions due to the use of different global analyses (after an objective reanalysis of standard sounding and surface observations) thus constitutes a realistic initial condition uncertainty for the limited area model forecasts (Zhang *et al*., 2002, 2006). This section first examines the influence of deriving initial conditions from global analyses of two different operational centres on the prediction of this heavy precipitation event. This is followed by an in-depth investigation of the sensitivity of error growth to the amplitude and scales of such realistic initial uncertainties.

5.1. Sensitivity to initial data sources

As in Table I, experiment 'T106ic' is identical to CNTL (including the use of the same boundary conditions) except that the $1.125^\circ \times 1.125^\circ$ T106 global analyses from the Chinese National Meteorological Centre (NMC) were used to derive the initial conditions (also with the standard objective reanalysis of standard observations). From the 24-h accumulated precipitation (>25 mm shaded) of T106ic and the corresponding difference from CNTL (Figure 5(a)), it was found that the forecast difference of precipitation with a 36-h lead-time was extremely large. In many localized regions, the difference is comparable in magnitude to the control simulation (CNTL). The 24-h accumulated precipitation belts in T106ic were systematically ~200 km further west and 200 km further south than those in CNTL (refer to Figure 1(b)). The 500-hPa wind and temperature difference between T106ic and CNTL also showed a moderate error growth in amplitude from 0 (Figure 6(a)) to 24 h (Figure 7(a), showing the same domain as the small box in Figure 6). The large forecast sensitivity to such realistic initial uncertainties thus implies limited mesoscale predictability using deterministic forecasts of the heavy precipitation associated with the Mei-Yu front. This is consistent with the results of Zhang *et al*. (2002, 2006).

Boundary condition uncertainties may also be an important source of error for limited area forecasts (Laprise *et al*., 2000). Although the primary region of interest (the heavy precipitation near Wuhan area) is far away from the lateral boundaries, there is still a noticeable reduction in the 24-h accumulated precipitation (when compared with CNTL) in an experiment ('T106bc') identical to CNTL except that the NMC global analyses were used to provide the boundary conditions (not shown). Nevertheless, due to the use of a large forecast domain, the difference when using different lateral boundary conditions was significantly smaller than that when using different initial conditions derived from different global analyses.

To further quantify the initial condition and forecast divergence between different experiments, this study used the domain-integrated difference total energy (DTE), as defined by Zhang *et al*. (2002):

$$DTE = \frac{1}{2}\sum(U_{ijk}^{'\,2} + V_{ijk}^{'\,2} + \kappa T_{ijk}^{'\,2}), \qquad (1)$$

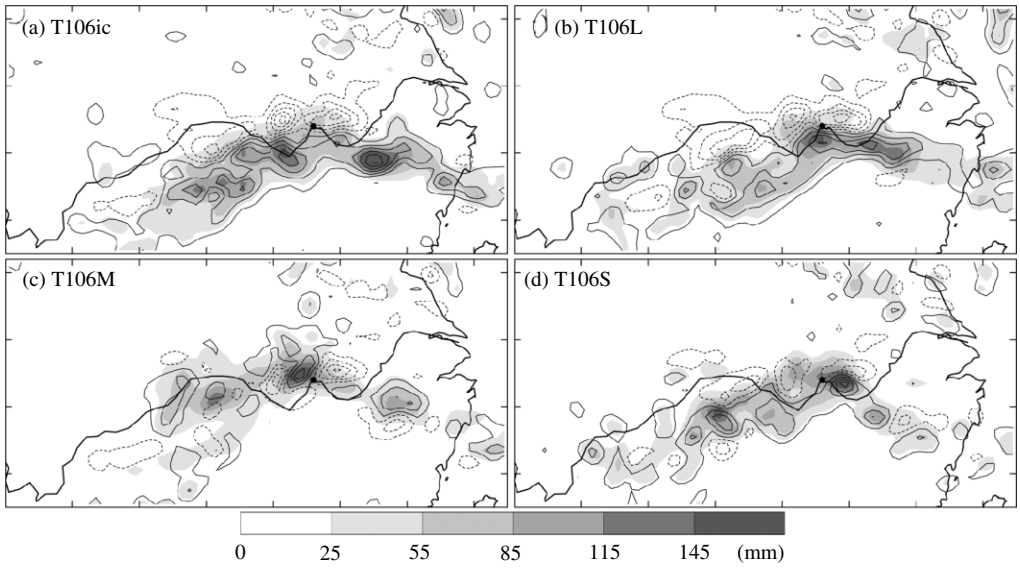

Figure 5. The simulated 24-h accumulated precipitation (mm, shaded) from 12:00 UTC 20 to 12:00 UTC 21 July 1998 by experiments (a) T106ic, (b) T106L, (c) T106M and (d) T106S plotted on the 30-km domain (D1) and the corresponding difference from CNTL (contoured every 30 mm).

DOI: 10.1002/qj

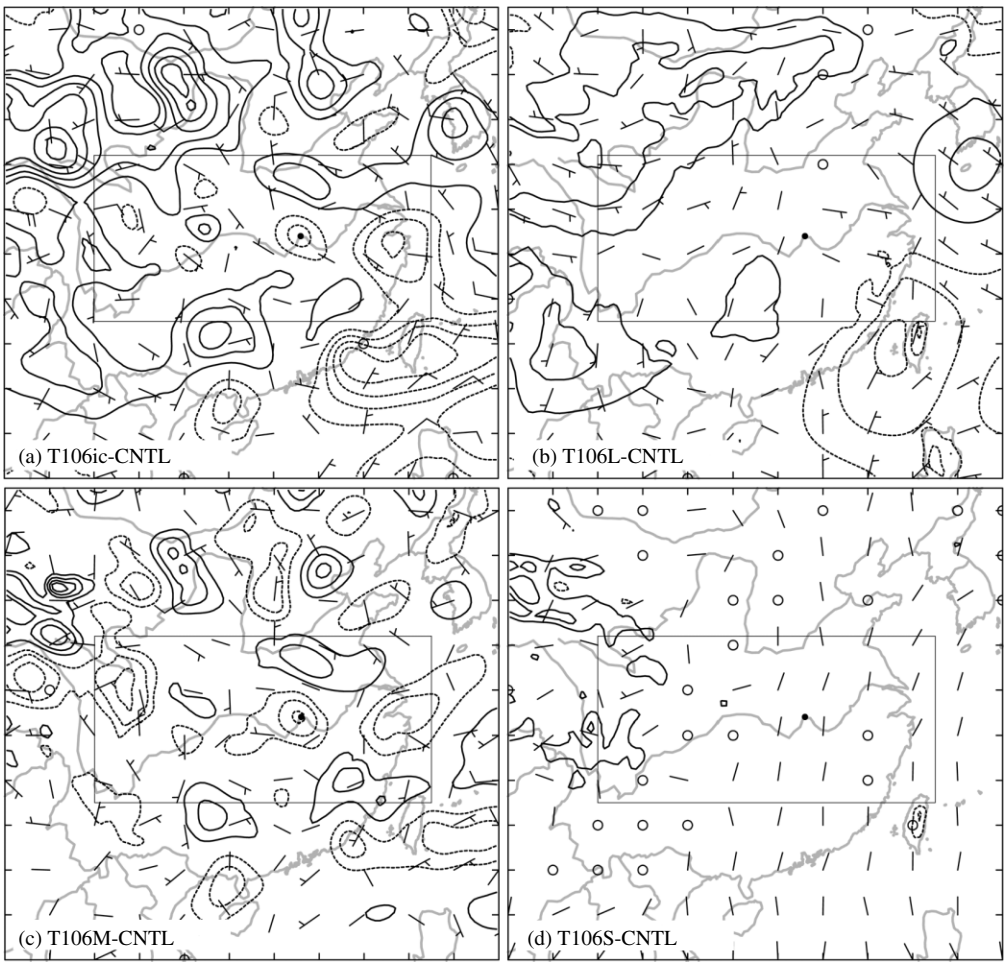

Figure 6. The 500-hPa wind (full barb, 5 m s^{-1}) and temperature (every 0.5 K; dashed, negative) difference between CNTL and experiments (a) T106ic, (b) T106L, (c) T106M and (d) T106S at the model initial time. The inner box in each panel denotes location of the display domain of Figure 7.

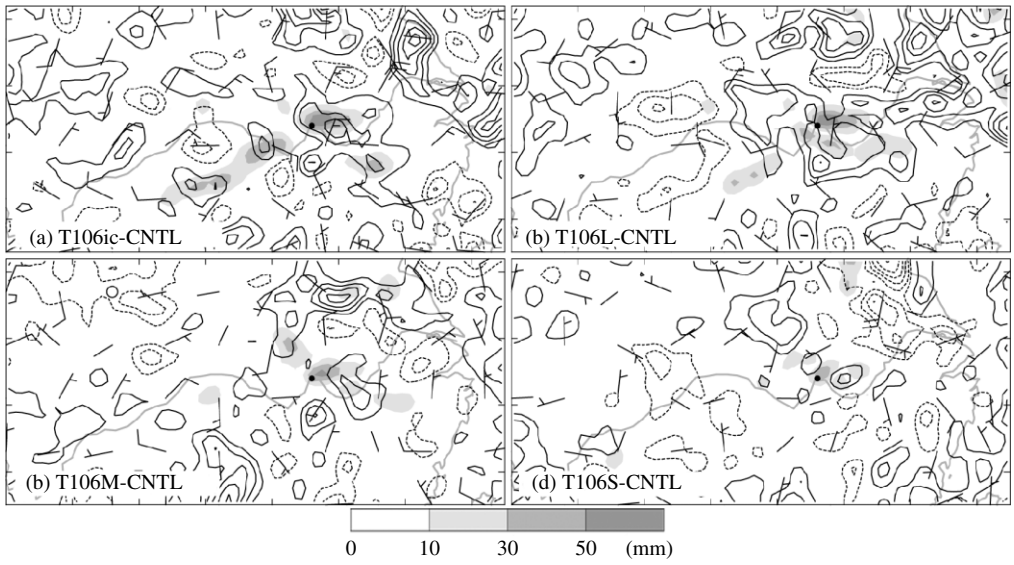

Figure 7. The 500-hPa wind (full barb, 5 m s^{-1}) and temperature (every 0.5 K; dashed, negative) difference between CNTL and experiments (a) T106ic, (b) T106L, (c) T106M, (d) T106S valid at 00 : 00 UTC 21 July (with a 24-h lead time) and the corresponding 3-h accumulated precipitation difference (every 20 mm, >10 mm shaded).

DOI: 10.1002/qj

where U', V' and T' are the wind component and temperature differences between two simulations, $\kappa = C_p/T_r$, T_r is the reference temperature and i, j and k run over x, y and z grid points.

Time evolutions of DTE between CNTL and the three aforementioned sensitivity experiments with respect to realistic uncertainties in initial conditions (T106ic), boundary condition (T106bc) and model resolution (C30KM) are summarized in Figure 8(a). In agreement with the precipitation forecast difference discussed above, the DTE errors induced by realistic initial uncertainties are much bigger than those induced by the other two sources (i.e. boundary conditions and model resolution). This is especially true for the first 24 h of the simulations. Despite a relatively small overall growth of the domain-integrated DTE between CNTL and T106ic, the DTE is ~30% larger than the difference between CNTL and T106bc, and twice as large as that between CNTL and C30KM at the 36-h forecast time. This further suggests that the initial condition uncertainties remain one of the most important sources of short-range mesoscale forecast errors for this heavy precipitation event.

The initial difference between CNTL and T106ic was concentrated mainly at larger scales. While there was little or no growth of the DTE error at larger scales (>600 km) over the 36-h simulation, there was a great increase at smaller scales (<600 km), with apparent error saturation at the smallest resolvable scales (<200 km) (Figure 9(d)).

5.2. Sensitivity to initial perturbations at different scales

Because the evolution and spectral analyses of the DTE error between CNTL and T106ic examined in the above subsection showed an apparent dependence of error growth on the scale and amplitude of the initial perturbations, we next used 2D spectral decomposition to divide the initial difference between CNTL and T106ic into three scales. Wavelengths of smaller-scale perturbations were less than 300 km, those of larger-scale perturbations were greater than 1200 km and the intermediate-scale perturbations were between 300 km and 1200 km. These three different scales of perturbations were then added to the CNTL initial conditions for sensitivity experiments 'T106L', 'T106M' and 'T106S', which were otherwise performed identically to CNTL and T106ic (note that all initial perturbations for any experiment herein are applied to the 30-km coarse grid and then interpolated to the nested domain). These sensitivity experiments were designed to further examine the influence of initial perturbations with different scale characteristics on the error growth process. An example of decomposed 500-hPa winds and temperature initial perturbations at different scales is shown in Figure 6(b)–(d). In terms of domain-averaged root-mean DTE (RM-DTE), the amplitude of large-scale perturbations in T106L (~2.3 m s^{-1}) was slightly larger than that of T106M (~2.0 m s^{-1}), and the perturbations in T106M were more than two times stronger than those of T106S (~1.0 m s^{-1}). It is not surprising that most of the initial difference between T106ic and CNTL (~3.0 m s^{-1}) came from larger and intermediate scales (>300 km), since the first guesses of the initial conditions for both experiments were derived from different coarse-resolution global analyses.

Figure 5(b)–(d) shows the 24-h accumulated precipitation simulated by T106L, T106M and T106S (>25 mm shaded) and the corresponding difference from CNTL. The experiment with truncated larger-scale perturbations (T106L) produced the largest error (i.e. difference from CNTL) in the precipitation forecast. Both the scale and amplitude of the differences were comparable to those between T106ic and CNTL (Figure 5(a) *vs* Figure 5(b)). The 24-h accumulated precipitation belt along the Yangtze river basin was systematically dislocated to the south in T106L (Figure 5(b)). The maximum 24-h accumulated precipitation differences near the Wuhan area between CNTL and T106L, T106M and T106S were respectively 130, 119 and 100 mm. It is obvious that precipitation errors in T106M and T106S are comparable in magnitude and scale, and both experiments also resulted in significant changes in amplitude and location of the precipitation maximum near Wuhan (Figure 5(c)–(d)).

The time evolution of the root-mean-square (RMS) of the 3-h accumulated precipitation differences (hereafter RMS-RAIN) between the perturbed experiments (i.e. T106ic, T106L, T106M, T106S) and CNTL averaged

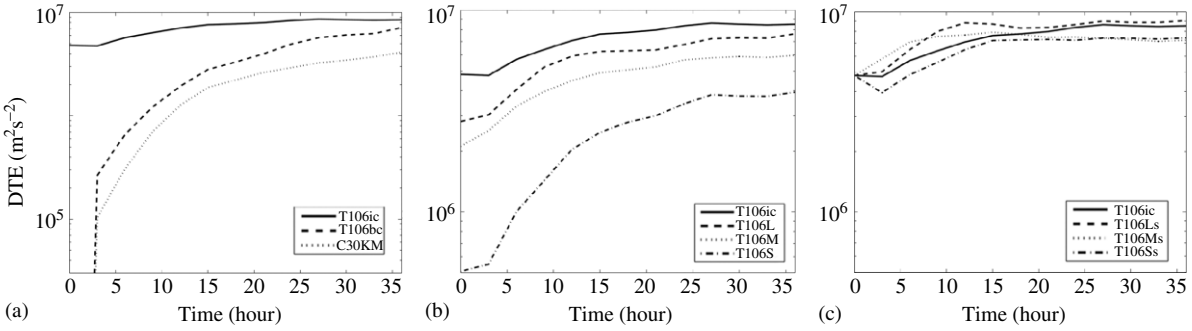

Figure 8. The time evolution of the domain-integrated difference total energy (DTE, m^2 s^{-2}) between CNTL and experiments (a) T106ic, T106bc and C30KM, (b) T106ic, T106L, T106M and T106S, and (c) T106ic, T106Ls, T106Ms and T106Ss.

DOI: 10.1002/qj

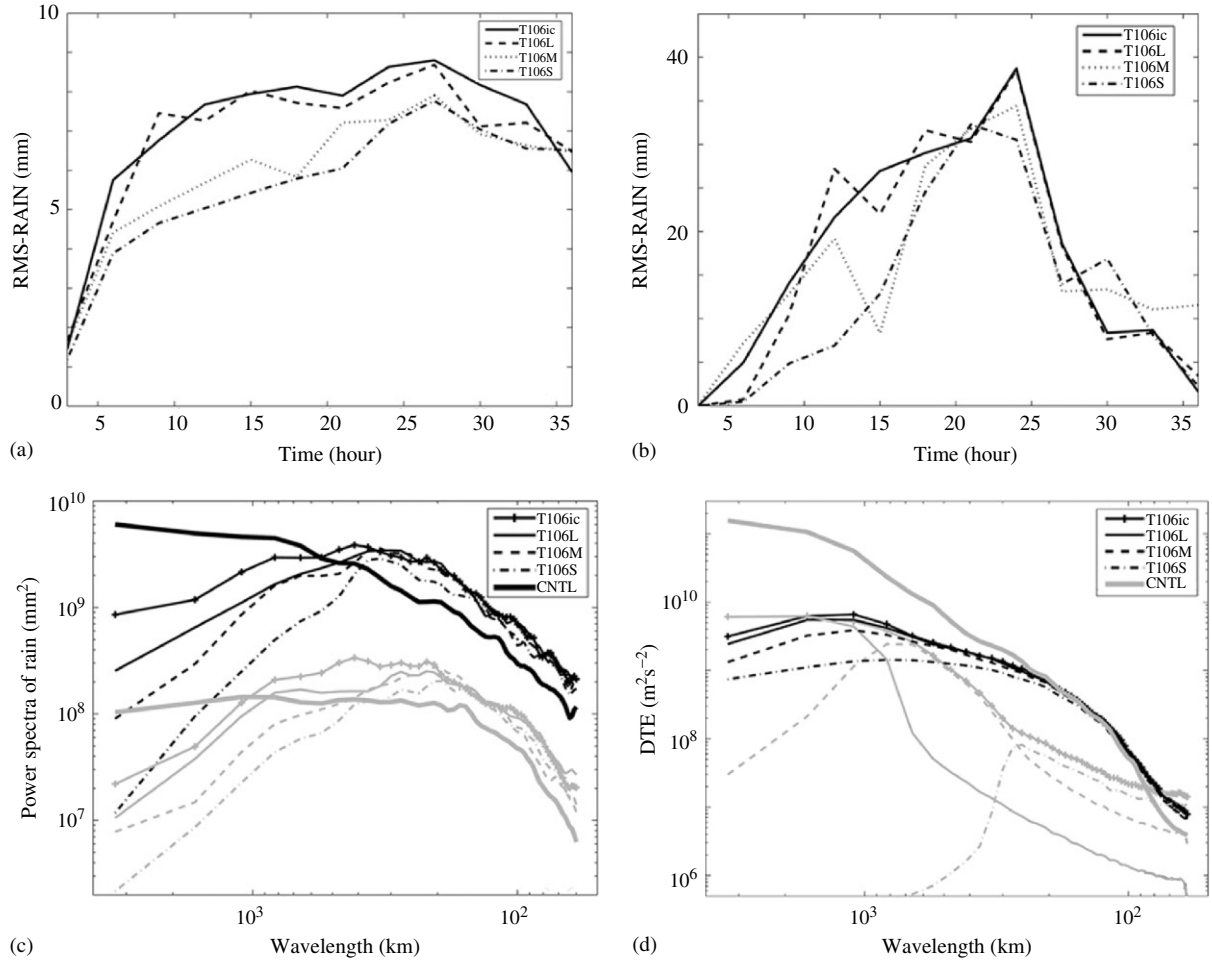

Figure 9. (a) The time evolution of the root-mean-square difference of 3-h accumulated precipitation (mm) between CNTL and experiments T106ic, T106L, T106M, T106S averaged over domain 1 (D1) from 00 : 00 UTC 20 to 12 : 00 UTC 21 July 1998; (b) as in (a) but averaged over the small rectangular box near Wuhan (denoted in Figure 1(a)); (c) the power spectra of the 3-h (grey) and 24-h (black) accumulated precipitation difference (mm^2) between CNTL and the above four experiments valid at the 24- and 36-h forecast times, respectively; (d) the power spectra of DTE (m^2 s^{-2}) between CNTL and the above four experiments at 0 h (grey) and 36 h (dark), respectively. The thick curves in (c–d) denote the corresponding full spectrum in CNTL.

over the entire D2 and the rectangular box (small box in Figure 1(a)) around Wuhan are shown in Figure 9(a)–(b) respectively. The 3-h RMS-RAIN error by T106M and T106S were similar over D2, a result that is consistent with the 24-h accumulated precipitation differences shown in Figure 5. Both T106M and T106S exhibited 15–30% smaller error than that of T106L and T106ic for the first 24-h simulation, but the amplitude of their errors converged to a similar value at 36 h (Figure 9(a)). On the other hand, the 3-h RMS-RAIN error in the box around Wuhan was comparable in magnitude after 18 h in all four experiments (Figure 9(b)). This corresponds to the time right before the onset of the peak precipitation in this area (Figure 2). Since the large forecast error of precipitation over the Wuhan area is a result of initial condition uncertainties and is independent of their initial scale and amplitude, deterministic QPF for localized heavy precipitation is exceptionally difficult.

From the spectral analysis of 3-h accumulated precipitation difference valid at 24 h and the 24-h accumulated precipitation difference valid at 36 h (Figure 9(c)), it was found that precipitation differences between these experiments (T106ic, T106L, T106M and T106S) and CNTL occurred mostly at scales between 200 and 600 km and peaked at ~400 km. In all experiments, the 3-h accumulated precipitation errors valid at 24 h were saturated at scales smaller than 400 km. Also, the precipitation differences were increasingly large at larger scales. On the other hand, the 3-h accumulated precipitation differences valid at 36 h between all the experiments and CNTL were quite similar at all scales (not shown). In terms of daily accumulated precipitation forecast, the error energy of the 24-h accumulated precipitation differences valid at 36 h between the above experiments and CNTL were very similar and were all larger than the spectrum of the total precipitation in CNTL at scales smaller than ~400 km. This implies a complete loss of predictability of precipitation at smaller scales. Again, the error at scales larger than 400 km increased from smallest to largest, respectively, in T106S, T106M, T106L and T106ic. The error in all these experiments at the larger scales was smaller than that of the total precipitation spectrum in CNTL (implying the ability of prediction at these large scales).

DOI: 10.1002/qj

The 500-hPa wind and temperature differences and the 3-h accumulated precipitation difference between these experiments (T106ic, T106L, T106M and T106S) and CNTL valid at 00:00 UTC 21 July (with a 24-h lead time, i.e. the observed peak period of heavy precipitation near Wuhan) are displayed in Figure 7. As with the precipitation difference, the wind and temperature errors for T106L and T106ic are comparable in magnitude. Both are significantly larger in scale and magnitude than those in T106M and T106S. It is worth noting that, unlike in Zhang *et al*. (2006), the largest error in these sensitivity experiments does not necessarily collocate directly with the maximum precipitation difference.

To further quantify the error growth between experiments with initial perturbations at different scales and CNTL, the time evolution and spectral distribution of the domain-integrated DTE were examined. In agreement with the initial amplitude difference, the DTE error in T106L (induced by truncated larger-scale perturbations) was smaller than that in T106ic (with initial uncertainties in all scales) but was consistently larger than that in T106M and T106S (induced by smaller and intermediate-scale uncertainties) throughout the 36-h simulations (Figure 8(b)). Except for the first few hours, the error growth rate of T106S, which has the smallest initial amplitude, was significantly larger than that of T106M and T106L for the first 24-h simulations. After 24 h, the growth rates of these three experiments and T106ic became very similar. By 36 h, the DTE error between T106L and CNTL approached that between T106ic and CNTL. This implies that the error growth due to larger-scale initial uncertainties (in terms of the DTE amplitude) is most significant. Nevertheless, the error growth due to smaller or intermediate-scale initial uncertainties is also quite significant at and beyond the 24-h forecast time (Figure 8(b)).

Figure 9(d) also shows the spectral distribution of the DTE error between each of the above three truncated initial perturbation experiments and CNTL at 0- and 36-h forecast times. In all experiments, there was a rapid initial error growth at the scales that are initially truncated off (not shown). The error energy between CNTL and T106L increases rapidly at smaller and intermediate scales (<1200 km, scales at which errors were truncated initially) but later approaches a level of saturation. The error energy between CNTL and T106M (T106S) also increases rapidly at larger and smaller (larger and intermediate) scales for the first 24 h (not shown). Between 12 and 24 h, the DTE spectra between CNTL and these three experiments all approach a level of saturation at scales smaller than 600 km, and differences are increasingly larger at larger scales. It is worth noting that there is a slight DTE error decrease between T106L and CNTL at larger scales (>1200 km) after 36-h integration. This is also the case for T106ic, and could be a sign of weakening larger-scale instability at the end of the simulations.

The similarity of the 36-h DTE difference between T106L and CNTL to that between T106ic and CNTL implies that improving the analysis at smaller to intermediate scales (<1200 km) would not significantly improve the 36-h forecast accuracy at all scales. On the other hand, despite apparent upscale error growth in T106M and T106S, limiting errors to only intermediate or smaller scales by reducing larger-scale initial uncertainties may lead to significant improvement in larger-scale (>1200 km) forecasts. Similar results were also found by Tribbia and Baumhefner (2004), using the truncated wavelength perturbation in a global-scale numerical weather prediction model. However, even if the initial analysis errors are very small and limited only to small scales (<300 km) that are unavoidable with the current observational networks, there will be forecast errors at all scales that are comparable in magnitude (although still smaller) to errors induced by larger-scale initial uncertainties. The largest forecast error due to the small-scale, small-amplitude initial condition uncertainty occurs at the small to intermediate scales (300–1200 km). This has significant impacts on heavy precipitation forecasts and further implies the inherently limited predictability of this heavy precipitation event.

5.3. Rescaled initial perturbations at different scales

The above subsection investigated the forecast sensitivity to realistic initial condition uncertainties at different scales. However, these experiments have significantly different initial error amplitude because of the use of a spectral decomposition using *ad hoc* critical wavelengths for scale separation. This subsection examines the differences in error growth between experiments with initial perturbations at different scales but with the same amplitude (in terms of DTE). The initial perturbations of all model prognostic variables in T106L (T106M, T106S) were multiplied by the ratio of the initial root-mean DTE (RM-DTE) between T106ic and CNTL to that between CNTL and T106L (T106M, T106S). The rescaled initial perturbations in experiments 'T106Ls', 'T106Ms' and 'T106Ss' thus will all have the same initial amplitude as T106ic in terms of DTE.

Figure 10(a)–(b) shows the evolution of the RMS difference of the 3-h accumulated precipitation in these experiments with rescaled perturbations averaged respectively over D2 and the rectangular box around Wuhan. Compared with the precipitation difference in T106L, T106M and T106S, the RMS errors of the 3-h accumulated precipitation in T106Ls, T106Ms and T106Ss became similar to each other and to T106ic as early as 18 h. At earlier times (between 6 and 15 h), precipitation differences for T106Ls were largest, and they were smallest for T106Ms (Figure 10(a)). This is also generally true for RMS-RAIN over the heavy precipitation area around Wuhan (Figure 10(b)). The spectral analyses of the 3-h accumulated precipitation difference valid at 24 h and the 24-h accumulated precipitation difference valid at 36 h (Figure 10(c)) further show that the precipitation forecast differences are not only similar in magnitude (Figure 10(a)–(b)), but they are also

DOI: 10.1002/qj

quite similar in scale. The experiments with initial perturbations at smaller scales (T106Ss, T106Ms) still have smaller errors at larger scales (>1200 km) but the difference is much smaller than those of T106S and T106M. The 3-h accumulated precipitation errors valid at 24 h in all experiments exceed the spectral energy of the total CNTL precipitation at scales below ~600 km while the 24-h accumulated precipitation errors valid at 36 h saturates at scales below ~500 km (Figure 10(c)). This indicates a complete loss of predictability at these scales. These results suggest that larger initial errors, even at smaller scales, can be detrimental to the QPF forecast.

As for the precipitation forecast difference discussed above, the domain-integrated DTE error between the rescaled-perturbation experiments and CNTL was also very similar in amplitude throughout the simulation (Figure 8(c)). The spectral analyses of the DTE at the initial and 36-h forecast times show that the error energy in all rescaled-perturbation experiments has a rapid initial growth at the scales which are initially truncated off (as in the experiments described in Section 5.2) but a drop of varying degrees at the scales of the initial peak spectra (not shown). At 36 h, the DTE spectra at all scales were similar to that between T106ic and CNTL, and all had apparent error saturation at scales smaller than 300 km after 24 h of simulation. The DTE evolution and spectral analyses further demonstrate the significance of smaller-scale but large-amplitude initial perturbations to the short-range mesoscale forecasts.

6. Sensitivity to random, idealized initial perturbations

The previous section examined the impacts of initial perturbations at different scales and amplitudes on the mesoscale predictability of this extreme precipitation event. These uncertainties originated from using different global analyses as initial analyses and are quite realistic in current operational systems. They thus demonstrate a practical limit of predictability on our short-range mesoscale forecast (Zhang *et al.*, 2006). To further examine the forecast sensitivity to the scales and amplitudes of the initial perturbations, two forms of idealized, random perturbations with different amplitudes are used in this section.

6.1. Idealized perturbations with realistic initial amplitude

Experiment 'BAL' uses the initial perturbation fields derived from the larger-scale and balanced background

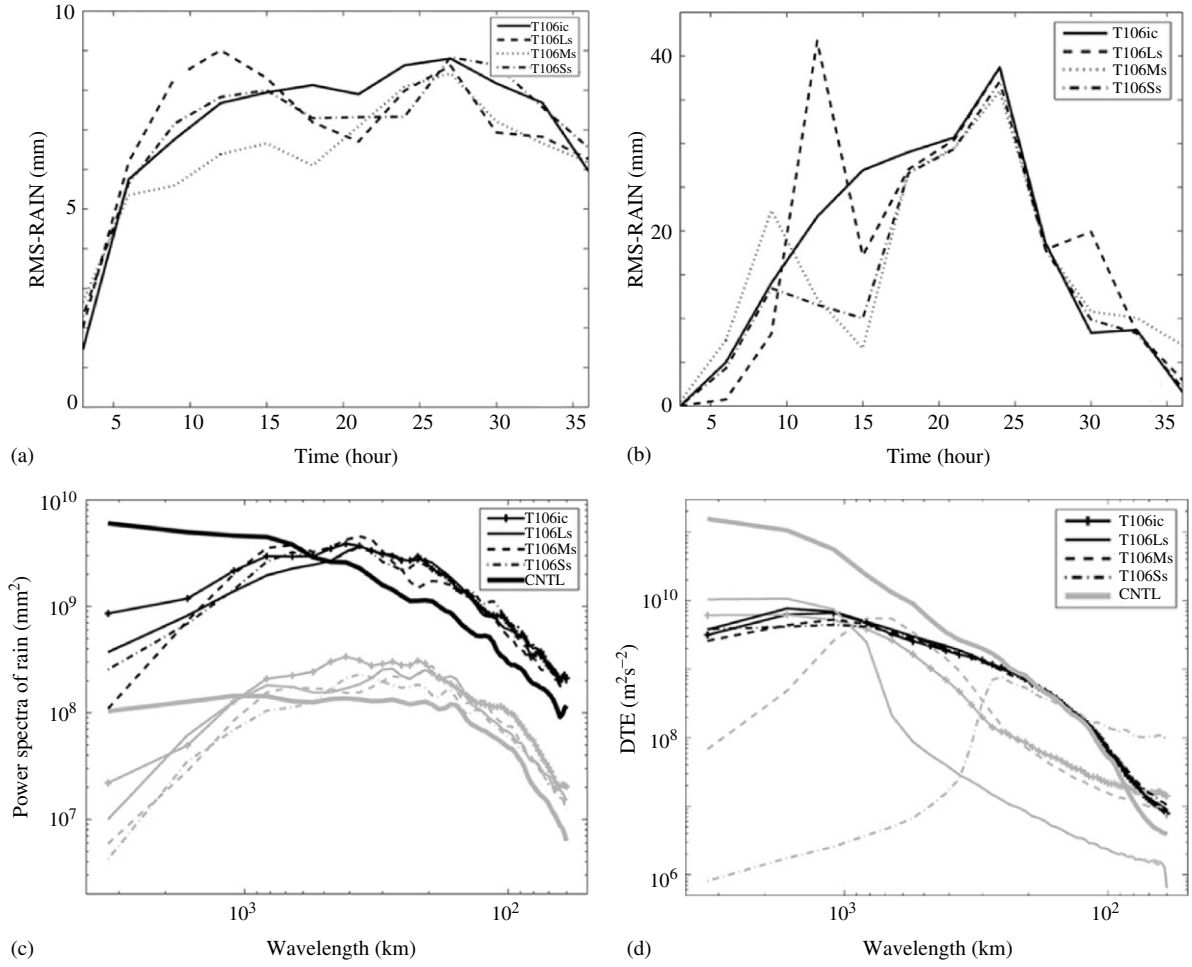

Figure 10. As in Figure 9 but for differences between CNTL and experiments T106ic, T106Ls, T106Ms and T106Ss.

DOI: 10.1002/qj

error covariance of the MM5 3Dvar system (Barker *et al*., 2004). The balance between mass and wind increments is achieved via a geostrophically and cyclostrophically balanced pressure perturbation from the wind analysis increments. A statistical regression is used to ensure the balance is used only where it is appropriate (Barker *et al*., 2004). The amplitude of the initial perturbations in BAL is scaled to match the difference between T106ic and CNTL in terms of DTE. Experiment 'UNB', which contains the same initial DTE amplitude as that in BAL, uses mostly smaller-scale and unbalanced 'grid-point' Gaussian noise in the initial temperature and wind fields (Zhang, 2005). The temperature and wind fields, respectively, have standard deviations of 1.225 K and 2.45 m s^{-1} throughout the model domain.

Since BAL uses the same amplitude perturbation as T106Ls, which is also perturbed mostly at larger scales, the domain-integrated DTE error in BAL (Figure 11(a)) and its spectral distribution (Figure 12(d)) are very similar to those in T106Ls (Figures 8(c) and 10(d)) throughout the entire simulation period. Since the error evolution resulting from the idealized and random perturbations in BAL is similar to that in T106Ls, the results of T106Ls can be generalized using the rescaled and filtered large-scale perturbation.

While UNB used perturbations concentrated at smaller scales with the same amplitude as those in T106Ss, after the initial time its domain-integrated DTE error (Figure 11(a)) and spectral distribution (Figure 12(d)) were very similar to those in T106S (Figures 8(b) and 9(d)) instead of T106Ss (Figures 8(c) and 10(d)). This discrepancy arises because the use of purely random grid-point noise introduces excessive perturbation energy (much larger than the total energy at these scales) at the smallest resolvable scales in UNB. This excessive amount of unbalanced perturbation energy at smaller scales is quickly removed by model diffusion and/or geostrophic adjustment (see Snyder *et al*., 2003; Zhang, 2005). Thus the effective perturbation amplitude of UNB (and subsequent evolution) is indeed more similar to T106S than to T106Ss. While Figure 10(d) shows that T106Ss also exhibits some excessive initial perturbation energy at the smallest scale, these perturbations are much less pronounced than those in UNB.

Figure 13(a)–(b) shows the 24-h accumulated precipitation simulated by the above two idealized-perturbation experiments and the corresponding differences from CNTL. The maximum 24-h accumulated precipitation difference between BAL (UNB) and CNTL is 107 (90) mm near Wuhan. This is slightly smaller than that between T106Ls (T106S) and CNTL and is consistent with the DTE evolution. The RMS-RAIN between BAL (UNB) and CNTL (Figure 12(a)–(b)) is very similar to that between T106Ls (T106S) and CNTL (Figures 10(a)–(b) and 9(a)–(b)) in both magnitude and evolution. The spectrum of the 3-h (24-h) accumulated precipitation difference between BAL (UNB) and CNTL (Figure 12(c)) valid at 24 h (36 h) is also similar in distribution and comparable (slightly smaller) in magnitude to that between T106Ls (T106S) and CNTL (Figures 10(c) and 9(c)). Consistent with the precipitation difference and DTE evolution, the magnitudes of the 500-hPa wind, temperature and the 3-h accumulated precipitation differences between BAL (UNB) and CNTL valid at 24 h are also similar to those between T106Ls (T106S) and CNTL.

6.2. Smaller-amplitude idealized perturbations

Experiments 'BAL27%', 'BAL9%' and 'BAL3%' ('UNB27%', 'UNB9%' and 'UNB3%') were performed identically to BAL (UNB), but their initial perturbation amplitudes in terms of RM-DTE were respectively rescaled to 27%, 9% and 3% of that between BAL (UNB) and CNTL. UNB27%, UNB9% and UNB3% only use the 'grid-point', Gaussian noise in the initial temperature

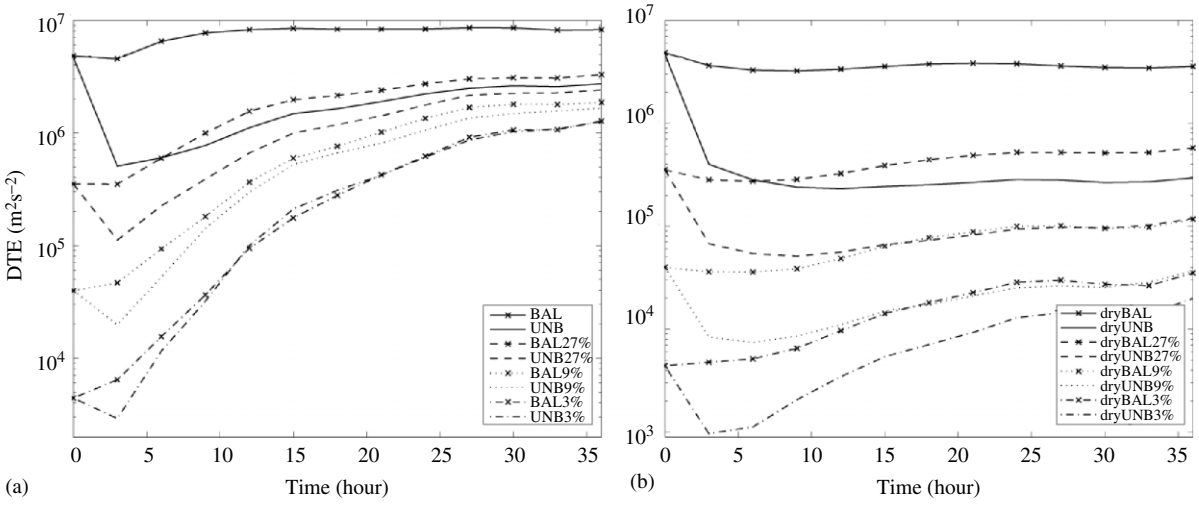

Figure 11. The time evolution of domain-integrated difference total energy (DTE, m^2 s^{-2}) (a) between CNTL and experiments with balanced or unbalanced idealized perturbations at different amplitude and (b) between dryCNTL and the other 'fake-dry' experiments. The name of each experiment is listed in figure keys.

DOI: 10.1002/qj

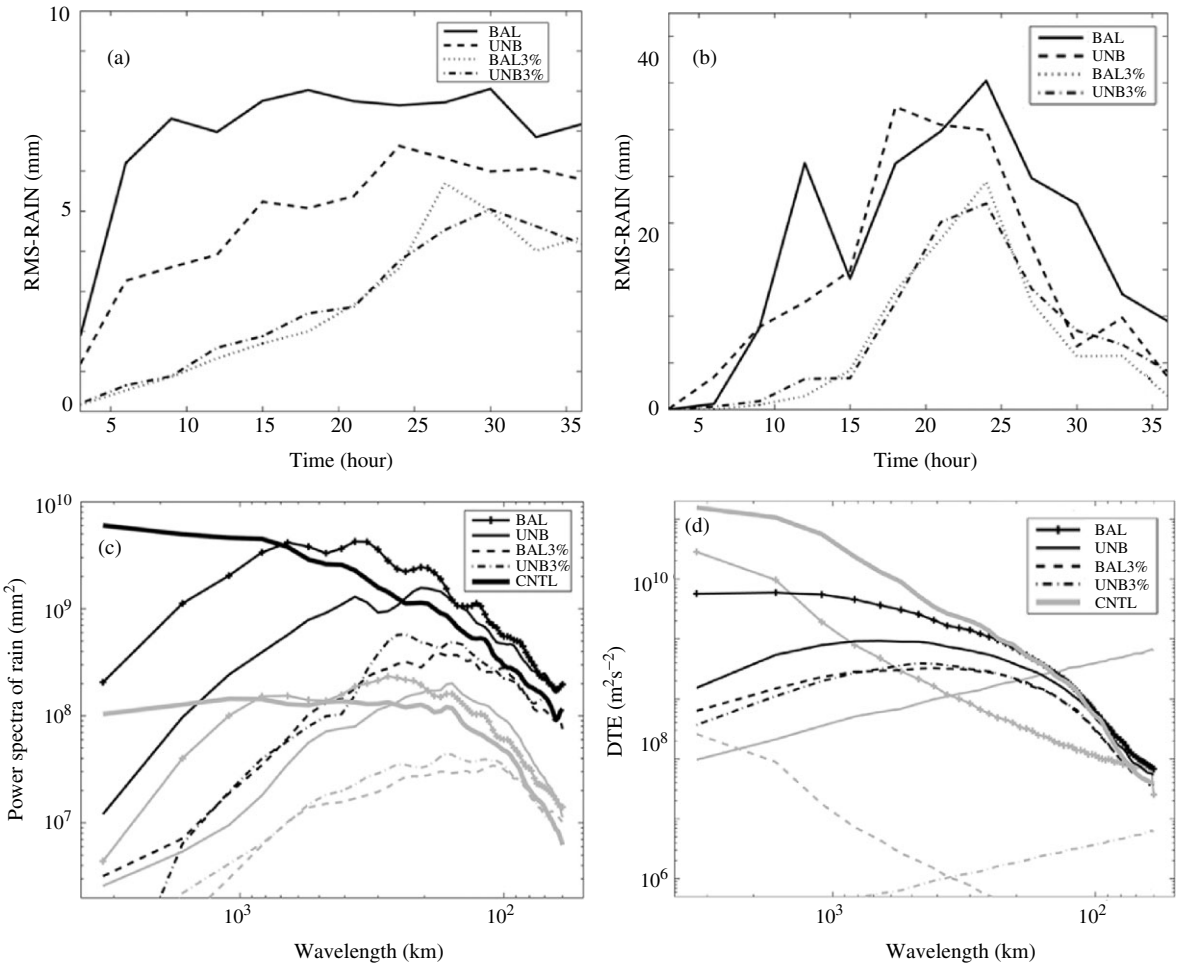

Figure 12. As in Figure 9 but for differences between CNTL and experiments BAL, UNB, BAL3%, UNB3%.

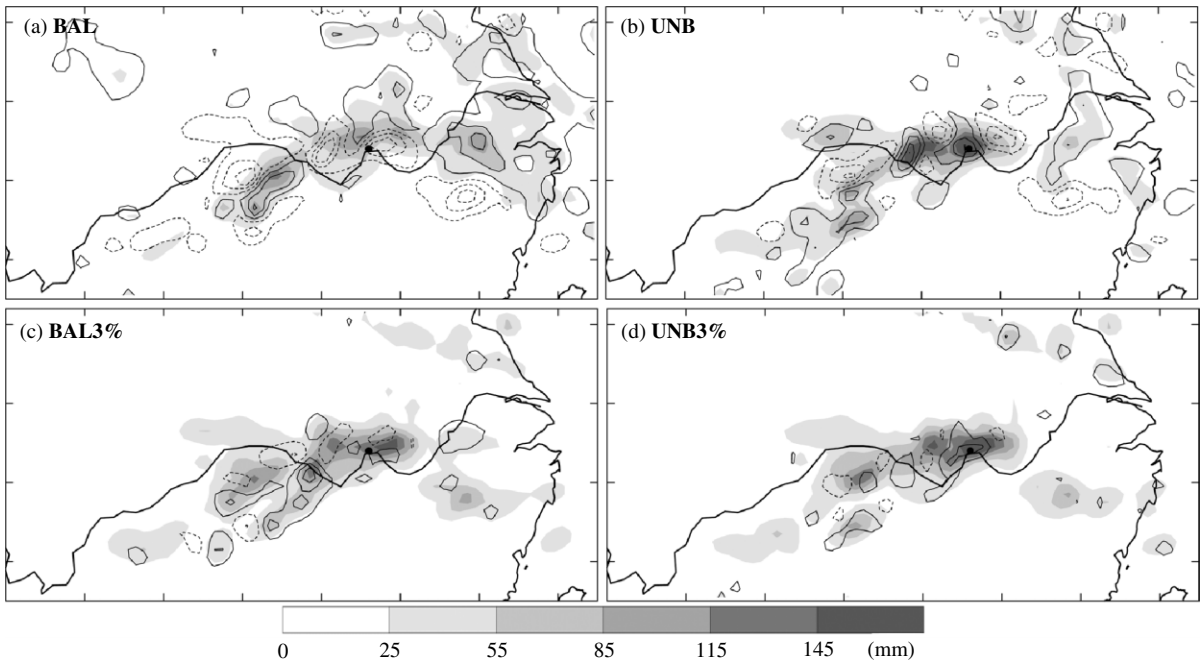

Figure 13. As in Figure 5 but for experiments (a) BAL, (b) UNB, (c) BAL3% and (d) UNB3%.

DOI: 10.1002/qj

field with respective standard deviations of 0.6, 0.2 and 0.07 K.

The maximum 24-h accumulated precipitation difference between BAL27%, BAL9%, BAL3%, UNB27%, UNB9%, UNB3% and CNTL decreased (though not linearly) with the decrease in initial perturbation amplitude. The 24-h accumulated precipitation simulated by BAL3%, UNB3% and the corresponding differences from CNTL are shown in Figure 13(c)–(d). As for the particular area near Wuhan, the maximum 24-h accumulated precipitation difference induced by smaller-scale, unbalanced perturbations was larger than that induced by larger-scale, balanced perturbations. For example, the maximum 24-h accumulated precipitation difference near Wuhan between UNB27% (UNB9%) and CNTL was ~129 (80) mm. This is obviously larger than that between BAL27% (BAL9%) and CNTL, which was ~68 (42) mm. The above differences are all smaller than the maximum 24-h accumulated precipitation difference of ~150 mm between T106ic and CNTL, but they are still quite significant when compared with the observation maximum (286 mm). There was a further decrease in the amount of 24-h accumulated precipitation difference between BAL3% (UNB3%) and CNTL.

The evolutions of the RMS-RAIN difference in experiments BAL3% and UNB3% averaged over D2 and the rectangular box around Wuhan are respectively shown in Figure 12(a)–(b). The average D2 RMS-RAIN error induced by the larger-scale, balanced perturbations is always larger than that induced by the same-amplitude, smaller-scale, unbalanced perturbations during the peak precipitation period (from 21 to 27 h). However, the RMS-RAIN error is similar in amplitude at 36 h, especially for smaller-amplitude, initial-perturbation experiments (Figure 12(a)). Interestingly, for the boxed area near Wuhan (Figure 12(b)), RMS-RAIN induced by larger-scale, balanced perturbations is generally smaller than that induced by same-amplitude, smaller-scale, unbalanced perturbations (with the exception of UNB3% and BAL3% from 15 to 18 h and from 21 to 27 h). This is consistent with the maximum 24-h accumulated precipitation difference near Wuhan which was discussed above. The spectra of the 3-h (24-h) accumulated precipitation difference valid at 24 h (36 h) between CNTL and these ideally perturbed experiments (Figure 12(c)) are concentrated at the scales between 100 to 400 km and peak at ~150 km. The distributions are similar at different scales, and the magnitudes also increase with the initial perturbation amplitude.

The 500-hPa wind, temperature and 3-h accumulated precipitation differences between experiments BAL3% (UNB3%) and CNTL valid at 24 h are shown in Figure 14(c)–(d). Generally, larger (amplitude or scale) initial perturbations result in larger-magnitude wind and temperature differences. This further supports the findings from using realistic initial perturbation experiments examined in Sections 5.1–5.3. However, when the initial perturbation amplitude becomes sufficiently small, the forecast errors resulting from larger-scale, balanced and from smaller-scale, unbalanced initial perturbations with the same amplitude become very similar in both scale and amplitude (Figure 14(c)–(d)). For example, the maximum 500-hPa initial temperature perturbations in BAL9% and UNB9% are approximately 0.1 and 0.2 K (not shown). This is far beyond the accuracy of current observational networks. After 24 h of simulation (not shown), the 500-hPa errors in both BAL9% and UNB9% increase significantly to a maximum magnitude of ~2.0 K for temperature and ~3.0 m s^{-1} for wind. The maximum 3-h accumulated precipitation difference inside

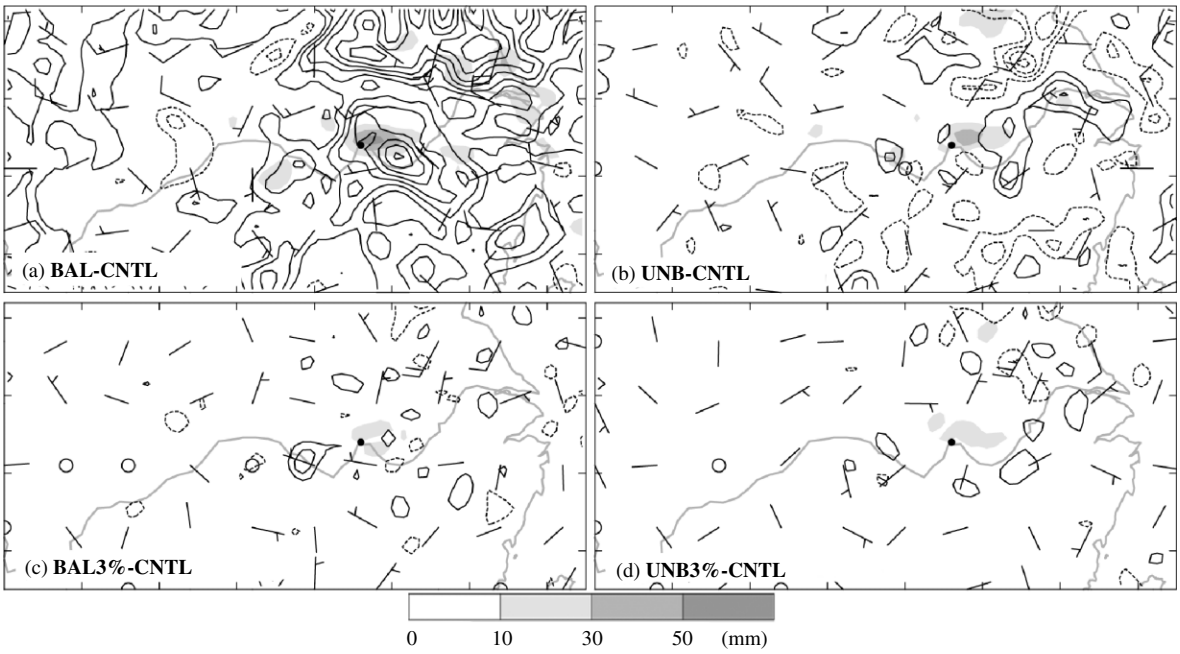

Figure 14. As in Figure 7 but for experiments (a) BAL, (b) UNB, (c) BAL3% and (d) UNB3%.

DOI: 10.1002/qj

the boxed area near Wuhan valid at 24 h is greater than 40 mm in both experiments. This is significant compared with the observed 3-h accumulated precipitation maximum of 150 mm. Slightly smaller sensitivities are also found with even smaller initial perturbations in experiments BAL3% and UNB3% (Figure 14(c)–(d)). These idealized experiments with small-amplitude initial perturbations at different scales further demonstrate the difficulty in the short-term prediction of this event and its localized heavy precipitation.

In agreement with the 500-hPa wind and temperature differences, the DTE error in experiments with larger-scale, balanced perturbations is larger than that in experiments with same-amplitude but smaller-scale, unbalanced perturbations (Figure 11(a)). The differences decrease with the decrease in initial perturbation amplitude and with the increase in simulation time. For example, the DTE errors in BAL3% and UNB3% become nearly the same after 18 h. The DTE errors in BAL27% and UNB27% become similar after 24 h, but the difference between BAL and UNB persists throughout the 36-h simulations (Figure 11(a)). Except for during the first few hours, the smaller-amplitude perturbation experiments also have faster error growth. These findings suggest that error growth in experiments with larger-scale, balanced initial errors is more linear than that with smaller-scale, unbalanced initial perturbations. It further demonstrates that, when the overall initial uncertainties are large, reducing initial errors at larger scales may lead to a significantly larger improvement in forecast, especially at larger scales (>1200 km). However, reducing errors at smaller scales would not significantly improve the 36-h forecast accuracy at all scales. This is further evidenced through examination of the DTE error spectra in these experiments (Figure 12(d)). Except for a decrease at the smallest resolvable scales for UNB27% and to a lesser degree in UNB, the DTE error in these experiments grows at all scales. Moreover, the DTE error in BAL27% (BAL9% and BAL3%) at scales smaller than 1000 km become similar to that of UNB27% (UNB9% and UNB3%) (e.g. Figure 12(d)).

6.3. 'Fake-dry' experiments

Nine 'fake-dry' experiments ('dryCNTL', 'dryBAL', 'dryUNB', 'dryBAL27%', 'dryUNB27%', 'dryBAL9%', 'dryUNB9%', 'dryBAL3%' and 'dryUNB3%') were identical to the full-moist experiments CNTL and BAL, UNB, BAL27%, UNB27%, BAL9%, UNB9%, BAL3%, UNB3% except that the diabatic heating and cooling from moist processes was turned off.

Figure 11(b) shows that error growth in all fake-dry experiments is greatly reduced when compared with the corresponding full-moist simulations with different initial perturbations (refer to Figure 11(a)). This is evidence of the strong dependence of error growth on moist dynamics (and possibly convective instability). However, the difference in DTE error between fake-dry and full-moist experiments with larger-scale, balanced initial perturbations (dryBAL, dryBAL27%, dryBAL9% and dryBAL3% *vs* BAL, BAL27%, BAL9% and BAL3%) was much smaller than that with smaller-scale, unbalanced perturbations (dryUNB, dryUNB27%, dryUNB9% and dryUNB3% *vs* UNB, UNB27%, UNB9% and UNB3%). This implies that the growth of smaller-scale unbalanced perturbations depends more on moist dynamics. Spectral analysis of the DTE error in the fake-dry experiments also shows that the DTE induced by the larger-scale, balanced perturbations is larger than that induced by the smaller-scale, unbalanced perturbations at all scales and that the error growth is apparently more linear without the influence of moist dynamics (not shown).

7. Discussion and conclusions

In this study, the impacts of initial condition errors on the mesoscale predictability of a summertime heavy precipitation event associated with the quasi-stationary Mei-Yu front were explored through various sensitivity experiments by using both realistic and idealized initial condition perturbations with different scales and amplitudes. It was found that larger-scale, larger-amplitude initial uncertainties generally led to larger forecast divergence than those with smaller scales and amplitudes.

Although the mesoscale model simulations initialized with ECMWF global analyses can reasonably depict the evolution of the synoptic-scale environment with a 36-h lead forecast time, there are still large variations between different experiments (i.e. C30KM, T106ic and T106bc) in the prediction of the mesoscale details and heavy precipitation of this event. The largest difference is found when comparing the predicted 24-h accumulated precipitation in T106ic and CNTL. A 2D spectral decomposition method is further used to divide the initial difference between CNTL and T106ic into three wavebands to be used as realistic perturbations at different scales. Examination of the evolution and spectral distribution of DTE indicates that larger-scale perturbations contribute the most to the strong forecast divergence introduced by using different initial data sources. However, the error due to smaller- or intermediate-scale initial uncertainties can also be quite significant beyond the 24-h forecast time. In terms of the daily accumulated precipitation forecast, the error energy spectra of the 24-h accumulated precipitation differences valid at 36-h between CNTL and the above three experiments is comparable to that of the total precipitation at scales smaller than 500 km. This implies a complete loss of predictability of precipitation at these smaller scales. Moreover, there are even large uncertainties in the deterministic forecast of localized or station-wise heavy precipitation regardless of the initial perturbation scale and amplitude. Experiments with initial perturbations at different scales that have been scaled to the same amplitude as the difference between T106ic and CNTL (in terms of DTE) suggest that larger initial errors, even at smaller scales, can be detrimental to the quantitative precipitation forecast.

DOI: 10.1002/qj

To generalize the results regarding the forecast sensitivity to the scale and amplitude of the initial perturbations, two forms of idealized, random perturbations (larger-scale, balanced perturbations *versus* smaller-scale, unbalanced perturbations) with different amplitudes are used. It is found that larger (amplitude or scale) initial perturbations induce larger (magnitude) wind and temperature differences. These idealized-perturbation experiments further demonstrate that when the overall initial uncertainties are large, reducing initial errors at larger scales may lead to significant improvement in forecasts, especially at larger scales (>1200 km). Also, reducing errors at smaller scales would not significantly improve the 36-h forecast accuracy at any scales. However, the errors induced by perturbations at different scales are similar if the initial amplitude is sufficiently small. Moreover, examination of the evolution of RMS precipitation error in a small area around Wuhan induced by these idealized perturbations shows that even if the amplitude of initial perturbations is very small, the predictability of such heavy precipitation events is still very limited, especially for the short-term precipitation. Findings obtained from the idealized-perturbation sensitivities experiments are consistent with results obtained from earlier realistic initial perturbation experiments.

It is worth noting that the current study only examined the mesoscale predictability of one Mei-Yu front heavy precipitation event. However, since the case examined occurred in a typical Mei-Yu synoptic environment and the observed heavy precipitation is typical for the Mei-Yu front, while the error grows with the background dynamics, especially moist convection, we believe that the conclusions drawn from this study are generic to this type of weather system. Moreover, the conclusions drawn from this study are broadly consistent with several previous studies (Zhang *et al*., 2003, 2006; Tan *et al*., 2004) on this subject. It is also found that error growth is strongly nonlinear. Smaller-amplitude initial errors, which are far smaller than those of current observational networks, may grow rapidly and quickly saturate at smaller scales. These errors subsequently grow upscale, leading to significant forecast uncertainties at increasingly larger scales. Moist convection is found to be the key to the rapid error growth that leads to limited mesoscale predictability. Error growth in the fake-dry simulations is greatly reduced compared to that of the corresponding moist simulations with initial perturbations at all amplitude and scales. However, error growth of smaller-scale, unbalanced initial perturbations is more sensitive to moist processes than is error growth of larger-scale, balanced perturbations. Complementary to the coarse-resolution, larger-scale study of Tribbia and Baumhefner (2004), the current study suggests that, while there is significant room to improve forecast skill by improving forecast models and initial conditions (especially the larger-scale component), mesoscale predictability of such a heavy precipitation event is inherently limited.

Acknowledgements

The authors are grateful to Jason Sippel and two anonymous reviewers for their comments on earlier versions of the manuscript. This research was funded by the US Office of Naval Research through the Young Investigator's Program (Award N000140410471). N.B. is also supported by the National Key Basic Research and Development Project of China (No. 2004CB418301).

References

Anthes RA, Kuo YH, Baumhefner DP, Errico RP, Bettge TW. 1985. Predictability of mesoscale atmospheric motions. *Adv. Geophys.* **28B**: 159–202.

Barker DM, Huang W, Guo Y-R, Bourgeois AJ, Xiao QN. 2004. A three-dimensional variational data assimilation system for MM5: implementation and initial results. *Mon. Weather Rev.* **132**: 897–914.

Bei N, Zhao S. 2002a. Mesoscale analysis of severe local heavy rainfall during the second stage of Mei-Yu season in 1998 (in Chinese). *Chin. J. Atmos. Sci.* **26**: 526–540.

Bei N, Zhao S. 2002b. The effect of initial field and physical processes on the heavy rainfall prediction of July 1998 (in Chinese). *Clim. Environ. Res.* **7**: 386–396.

Bei N, Zhao S, Gao S. 2002. Numerical simulation of a heavy rainfall event in China during July 1998. *Meteorol. Atmos. Phys.* **80**: 153–164.

Buizza R, Richardson DS, Palmer TN. 2003. Benefits of increased resolution in the ECMWF ensemble system and comparison with poor-man's ensembles. *Q. J. R. Meteorol. Soc.* **129**: 1269–1288.

Carbone RE, Tuttle JD, Ahijevych DA, Trier SB. 2002. Inferences of predictability associated with warm season precipitation episodes. *J. Atmos. Sci.* **59**: 2033–2056.

Chen Q-S. 1982. The instability of the gravity–inertia wave and its relation to low-level jet and heavy rainfall. *J. Meteorol. Soc. Jpn.* **60**: 1041–1057.

Chen GT-J. 1983. Observational aspects of Mei-Yu phenomena in subtropical China. *J. Meteorol. Soc. Jpn.* **61**: 306–312.

Chen S-J, Kuo Y-H, Wang W, Tao Z-Y, Cui B. 1998. A modeling case study of heavy rainstorms along the Mei-Yu front. *Mon. Weather Rev.* **126**: 2330–2351.

Ding Y-H. 1992. Summer monsoon rainfalls in China. *J. Meteorol. Soc. Jpn.* **70**: 373–396.

Done J, Davis C, Weisman M. 2004. The next-generation of NWP: cloud resolving forecasts with the weather research and forecasting (WRF) model. *Atmos. Sci. Lett.* **5**: 110–117.

Dudhia J. 1993. A nonhydrostatic version of the Penn State–NCAR mesoscale model: validation tests and simulation of an Atlantic cyclone and cold front. *Mon. Weather Rev.* **121**: 1493–1513.

Errico RM, Baumhefner DP. 1987. Predictability experiments using a high-resolution limited-area model. *Mon. Weather Rev.* **115**: 488–504.

Ehrendorfer M, Errico RM, Raeder KD. 1999. Singular-vector perturbation growth in a primitive equation model with moist physics. *J. Atmos. Sci.* **56**: 1627–1648.

Fritsch JM, Houze RA Jr, Adler R, Bluestein H, Bosart L, Brown J, Carr F, Davis C, Johnson RH, Junker N, Kuo Y-H, Rutledge S, Smith J, Toth Z, Wilson JW, Zipser E, Zrnic D. 1998. Quantitative precipitation forecasting: report of the Eighth Prospectus Development Team, U.S. Weather Research Program. *Bull. Am. Meteorol. Soc.* **79**: 285–299.

Gallus WA Jr. 2002. Impact of verification grid-box size on warm-season QPF skill measures. *Weather Forecasting* **17**: 1296–1302.

Grell GA. 1993. Prognostic evaluation of assumptions used by cumulus parameterizations. *Mon. Weather Rev.* **121**: 764–787.

Laprise R, Varma MR, Denis B, Caya D, Zawadzki I. 2000. Predictability of a nested limited-area model. *Mon. Weather Rev.* **128**: 4149–4154.

Lorenz EN. 1963. Deterministic nonperiodic flow. *J. Atmos. Sci.* **20**: 130–141.

Lorenz EN. 1969. The predictability of a flow which possesses many scales of motion. *Tellus* **21**: 289–307.

Lorenz EN. 1984. Estimates of atmospheric predictability in the medium range. *Predictability of Fluid Motions: AIP Conference Proceedings No 106*. American Institute of Physics, La Jolla Institute, pp. 133–140.

DOI: 10.1002/qj

Leith CE, Kraichnan RH. 1972. Predictability of turbulent flows. *J. Atmos. Sci.* **29**: 1041–1058.
Maxwell JC. 1876. *Matter and Motion*. (1952 edn), Dover, New York.
Mellor GL, Yamada T. 1982. Development of a turbulence closure-model for geophysical fluid problems. *Rev. Geophys.* **20**: 851–875.
Olson DA, Junker NW, Korty B. 1995. Evaluation of 33 years of quantitative precipitation forecasting at the NMC. *Weather Forecasting* **10**: 498–511.
Reisner J, Rasmussen RJ, Bruintjes RT. 1998. Explicit forecasting of supercooled liquid water in winter storms using the MM5 mesoscale model. *Q. J. R. Meteorol. Soc.* **124**: 1071–1107.
Simmons AJ, Hollingsworth A. 2002. Some aspects of the improvement in skill of numerical weather prediction. *Q. J. R. Meteorol. Soc.* **128**: 647–677.
Snyder C, Hamill TM, Trier S. 2003. Linear evolution of error covariances in a quasigeostrophic model. *Mon. Weather Rev.* **131**: 189–205.
Tan Z, Zhang F, Rotunno R, Snyder C. 2004. Mesoscale predictability of moist baroclinic waves: experiments with parameterized convection. *J. Atmos. Sci.* **61**: 1794–1804.
Tribbia JJ, Baumhefner DP. 2004. Scale interactions and atmospheric predictability: an updated perspective. *Mon. Weather Rev.* **132**: 703–713.
Thompson PD. 1957. Uncertainty of initial state as a factor in the predictability of large scale atmospheric flow patterns. *Tellus* **9**: 275–295.
Vukicevic T, Errico RM. 1990. The influence of artificial and physical factors upon predictability estimates using a complex limited-area model. *Mon. Weather Rev.* **118**: 1460–1482.
Zhang F. 2005. Dynamics and structure of mesoscale error covariance of a winter cyclone estimated through short-range ensemble forecasts. *Mon. Weather Rev.* **133**: 2867–2893.
Zhang F, Snyder C, Rotunno R. 2002. Mesoscale predictability of the 'surprise' 24–25 January 2000 snowstorm. *Mon. Weather Rev.* **130**: 1617–1632.
Zhang F, Snyder C, Rotunno R. 2003. Effects of moist convection on mesoscale predictability. *J. Atmos. Sci.* **60**: 1173–1185.
Zhang F, Odins AM, Nielsen-Gammon JW. 2006. Mesoscale predictability of an extreme warm-season precipitation event. *Weather Forecasting* **21**: 149–166.
Zhao S, Sun J, Chen H, Zhang F. 1998. Diagnostic study of strong heavy rainstorm during the severe flooding at Yangtze River area at July 1998 (in Chinese). *Clim. Environ. Res.* **3**: 368–381.

DOI: 10.1002/qj